



Dynamic stiffness method for exact modelling of acoustics black hole beams using Meijer G-functions

Le Chang, Li Cheng^{*}

Department of Mechanical Engineering, The Hong Kong Polytechnic University, Hong Kong, China

ARTICLE INFO

Keywords:

Acoustic black hole
Dynamic stiffness method
Wittrick-Williams algorithm
Euler-Bernoulli beam
Meijer G-functions

ABSTRACT

The acoustics black hole (ABH) effect shows promising potential for wave manipulation and vibration control. An ABH structure features a gradual reduction of the phase velocity of flexural waves alongside wave compression and energy accumulation when entering the tapered ABH portion where the thickness is tailored according to a power-law (with power index m no less than 2). The corresponding non-uniform wavelength distribution over the ABH structure poses great challenges to conventional modelling methods. To alleviate the problem, this paper proposes an exact dynamic stiffness method for modelling ABH beams with arbitrary exponent equal to or greater than 2 under the framework of Euler-Bernoulli beam theory. For ABH with $m > 2$, a change of variable and the Mellin integral transformation are conducted to derive the integral representations of the exact solution using Meijer G-functions. The solution for the case with $m = 2$ is also derived for completeness. Then the dynamic stiffness matrix is formulated through symbolic operation. The Wittrick-Williams (WW) algorithm is revamped to cope with the ABH-specific requirement. Numerical examples are given to validate the solution in integral form, the dynamic stiffness matrix, and the efficacy of the improved WW algorithm. The clear advantage of the accurate integral representations over series representations is justified in the higher frequency range. Covering all ABH-relevant scenarios (with $m \geq 2$), the exact modelling framework established in this work offers a powerful tool for the modelling and investigation of more complex structures which are built upon ABH beam elements.

1. Introduction

Recent research on acoustic black holes points at enormous potential for the manipulation of flexural waves in structures, thus leading to exciting applications such as vibration control, sound radiation mitigation, energy harvesting, etc. As initially proposed by Mironov [1], an ABH structure, such as ABH beams/plates, features a decreasing thickness profile, which is tailored according to a power-law function $h = \epsilon x^m$ ($m \geq 2$). Theoretically, when incident flexural waves enter and propagate through the ABH portion, their phase velocity gradually reduces alongside shortened wavelength and drastically increased amplitude towards the ABH tip. At the ideal zero-thickness termination, where the wave speed theoretically becomes zero, no wave reflection would occur so that a perfect wave trap is achieved. Alongside this process is the compression of the wavelength and accentuation of high-density energy. In a more practical scenario where zero thickness is impossible to achieve, damping material [2] or energy harvesters [3,4] can be deployed to impair wave reflection and promote the ABH effects through absorbing or harvesting the concentrated energy. Numerous studies have

^{*} Corresponding author.

E-mail address: li.cheng@polyu.edu.hk (L. Cheng).

demonstrated that ABH effects can be capitalized for energy absorption and vibration reduction, as reported in a book [5].

Various modelling methods have been adopted for ABH studies and guiding structural designs based on ABH principles. The geometric acoustic method [1,2] treats the ABH as semi-infinite structures. This method concentrates on flexural wave propagation by analyzing the variations of local wave number and reflection coefficient, provided that the smoothness condition under the framework of geometric acoustics is satisfied. Other approaches were also utilized to investigate the ABH phenomena in more complex and realistic configurations, including the impedance matrix method [6,7], transfer matrix method [8–10], wavelet-based Rayleigh-Ritz method [11], finite difference method [12,13], finite element method (FEM) [14–16], partition of unity finite element method [17], and plane wave expansion method [18], etc.

Most numerical or semi-analytical methods, however, require a refined discretization scheme to accurately capture the strongly oscillatory behavior of the ABH. One of the salient features of an ABH structure is its unique and non-uniform wavelength distribution over the structure, especially within the ABH portion which is accentuated near the tip/indentation. Therefore, the local wavelength can drastically shorten in the high-frequency region, which would require a significant number of dense grids for those modelling methods based on discretization, leading to an exorbitant increase in computational costs. This problem becomes more apparent when dealing with more advanced ABH problems, such as the structural modelling with embedded ABH elements [19,20], passive vibration control with ABH absorbers [21,22], and optimal design of ABH profiles [23–25], etc. It is important to note that, even for relatively simple ABH elements such as a beam, most of the discretization-based methods can only deliver approximate solutions. For more complex ABH designs and assemblies, as more commonly seen in the realm of ABH-based meta-materials/structures, the aforementioned obstacles seem to be insurmountable under the existing modelling framework. Therefore, accurate and more effective simulation methods/tools need to be developed for ABH studies.

Unlike other approximation methods, the dynamic stiffness method (DSM) [26] is an exact method which can generate mesh-free results. This is owing to the exploitation of exact shape functions so that approximations can be avoided. As a result, no approximate expansion of the solution nor physical discretization of the structure is required, thus yielding the minimum number of degrees of freedom and high computational efficiency. This empowers the DSM with significant advantages in handling complex problems requiring repetitive computation. The use of the DSM in a series of beam elements has been attempted by Banerjee and other researchers [27–33]. However, few works on ABH structures exist in the context of DSM using the exact solution. An exception is the transverse wave of an ABH beam with $m = 2$ [34]. The cases with $m > 2$, however, were not considered in that work. Meanwhile, Jeon and Lee [35] derived the exact solution in series representation, namely, the generalized hypergeometric functions (HGF), instead of the dynamic stiffness matrix. Additionally, part of the alternative solutions of [35] contains series that are not integrated into mathematical software, which hinders the provision of the exact solution and compromises the computational efficiency. Moreover, series representations of solutions suffer from a clear disadvantage over integral representations when dealing with large values of the parameters [36] (which can be understood as higher frequency range in the context of structural dynamics). Finally, when handling derivative terms, series representations need a considerable amount of computation in both symbolic and numerical calculations, leading to unavoidable numerical error.

In this work, a general and efficient framework for the modelling of a Euler-Bernoulli ABH beams with arbitrary exponent $m \geq 2$ is developed based on the exact DSM. For cases with $m > 2$, Mellin integral transformation is applied to yield exact solutions expressed by the Meijer G-function, which is a line integral in the complex plane, to avoid series approximation. Then the dynamic stiffness (DS) matrix is derived through symbolic operation. For numerical implementation, the Wittrick-Williams algorithm is revamped for ABH beams. The proposed exact solutions cover all ABH-relevant cases with $m \geq 2$, thus offering a complete set of modelling tool for future ABH studies.

The paper is arranged as follows. In Section 2.1, the governing differential equation for an ABH beam with $m \geq 2$ is cast into an ordinary differential equation (ODE) containing function coefficients. A fundamental set of solutions represented by the Meijer G-functions are derived through Mellin integral transformation for cases with $m > 2$. In Sections 2.2, the continuous power index m is sorted into six cases for which alternative solutions are developed when the fundamental set of solutions are linearly dependent. To ensure the completeness of the solution set, the solution for ABH with $m = 2$ is also given. In Section 2.3, the DS matrix is formulated, which is subsequently used in Section 3 to perform dynamics analyses. Calculating procedures including steady-state response analysis

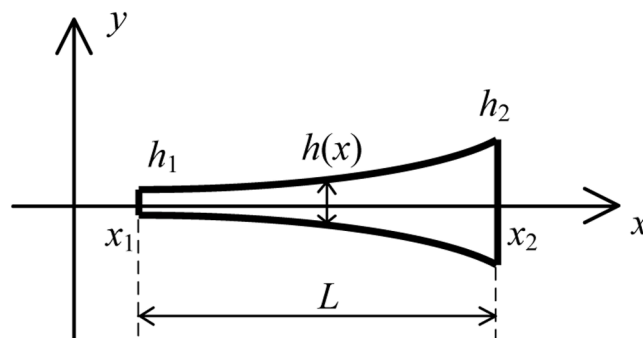


Fig. 1. A symmetrical ABH beam with $m \geq 2$.

and the improved Wittrick-Williams algorithm for computing the natural frequencies of non-uniform beams, are detailed. Dynamic analyses are then performed to validate the accuracy of the proposed method through comparisons with FEM results. Natural frequencies and mode shapes obtained from two models, DSM by Meijer G-functions (DSM-MG) and the one by hypergeometric functions (DSM-HG), are compared. Finally, Section 4 concludes the paper.

2. Exact dynamic stiffness method for ABH beam

2.1. Governing differential equations and fundamental solutions for an ABH beam with arbitrary exponent m

Flexural vibrations of an ABH beam whose thickness is described by $h(x) = \epsilon x^m (m \geq 2)$ as shown in Fig. 1 are governed by [27]

$$\frac{d^2}{dx^2} \left[D(x) \frac{d^2 W}{dx^2} \right] - \omega^2 \rho A(x) W = 0, \tag{1}$$

where x is the spatial coordinate; W the transverse displacement; ρ the mass density; E the Young's modulus. $D(x) = Ebh^3(x)/12$ is the local flexural rigidity of the beam; $A(x) = bh(x)$ is the cross-sectional area; and b the constant width of the beam. x starts from x_1 because of the inevitable truncation at the ABH tip end.

Substituting $h(x) = \epsilon x^m$ into Eq. (1) yields the following ordinary differential equation (ODE) with variable/function coefficients (since the coefficients in front of different derivative terms depend on variable x)

$$x^{2m} \frac{d^4 W}{dx^4} + 6mx^{2m-1} \frac{d^3 W}{dx^3} + 3m(3m-1)x^{2m-2} \frac{d^2 W}{dx^2} - \xi W(x) = 0, \tag{2}$$

where

$$\xi = 12\rho\omega^2/E\epsilon^2. \tag{3}$$

Performing the variable substitution

$$z = \frac{\xi}{(4-2m)^4} x^{4-2m}, \tag{4}$$

Eq. (2) can be rewritten in terms of z as

$$z^4 \frac{d^4 W}{dz^4} + 6 \frac{3-m}{4-2m} z^3 \frac{d^3 W}{dz^3} + \frac{m^2-25m+51}{(4-2m)^2} z^2 \frac{d^2 W}{dz^2} + \frac{(3-2m)(1+m)(2+m)}{(4-2m)^3} z \frac{dW}{dz} - zW(z) = 0, \tag{5}$$

which can be further condensed into the following form

$$\left[\left(z \frac{d}{dz} - \beta_0 \right) \left(z \frac{d}{dz} - \beta_1 \right) \left(z \frac{d}{dz} - \beta_2 \right) \left(z \frac{d}{dz} - \beta_3 \right) - z \right] W(z) = 0, \tag{6}$$

where

$$\beta_0 = 0, \beta_1 = \frac{1}{4-2m}, \beta_2 = \frac{2-3m}{4-2m}, \beta_3 = \frac{3-3m}{4-2m}. \tag{7}$$

We apply Mellin transform [37], defined by $F(\phi) = \mathcal{M}\{W(z), \phi\} = \int_0^\infty z^{\phi-1} W(z) dz$, to $W(z)$ to simplify Eq. (6), which yields the recursion equation (a detailed proof is given in Appendix A)

$$(\beta_0 + \phi)(\beta_1 + \phi)(\beta_2 + \phi)(\beta_3 + \phi)F(\phi) = F(\phi + 1), \tag{8}$$

where $F(\phi)$ is the Mellin transform of $W(z)$. Once Eq. (8) is solved, $W(z)$ can be obtained through inverse Mellin transform to $F(\phi)$. Since the gamma function $\Gamma(\phi)$ bears the property

$$\phi\Gamma(\phi) = \Gamma(\phi + 1), \tag{9}$$

we express the solution in terms of the gamma function, thus yielding eight possible solution forms for $F(\phi)$:

$$\begin{aligned}
 F_1(\phi) &= \frac{1}{\Gamma(1 - \beta_0 - \phi)\Gamma(1 - \beta_1 - \phi)\Gamma(1 - \beta_2 - \phi)\Gamma(1 - \beta_3 - \phi)}, \\
 F_2(\phi) &= \Gamma(\beta_0 + \phi)\Gamma(\beta_1 + \phi)\Gamma(\beta_2 + \phi)\Gamma(\beta_3 + \phi), \\
 F_3(\phi) &= \frac{\Gamma(\beta_0 + \phi)\Gamma(\beta_1 + \phi)}{\Gamma(1 - \beta_2 - \phi)\Gamma(1 - \beta_3 - \phi)}, F_4(\phi) = \frac{\Gamma(\beta_0 + \phi)\Gamma(\beta_2 + \phi)}{\Gamma(1 - \beta_1 - \phi)\Gamma(1 - \beta_3 - \phi)}, \\
 F_5(\phi) &= \frac{\Gamma(\beta_0 + \phi)\Gamma(\beta_3 + \phi)}{\Gamma(1 - \beta_1 - \phi)\Gamma(1 - \beta_2 - \phi)}, F_6(\phi) = \frac{\Gamma(\beta_1 + \phi)\Gamma(\beta_2 + \phi)}{\Gamma(1 - \beta_0 - \phi)\Gamma(1 - \beta_3 - \phi)}, \\
 F_7(\phi) &= \frac{\Gamma(\beta_1 + \phi)\Gamma(\beta_3 + \phi)}{\Gamma(1 - \beta_0 - \phi)\Gamma(1 - \beta_2 - \phi)}, F_8(\phi) = \frac{\Gamma(\beta_2 + \phi)\Gamma(\beta_3 + \phi)}{\Gamma(1 - \beta_0 - \phi)\Gamma(1 - \beta_1 - \phi)}.
 \end{aligned} \tag{10}$$

Applying the inverse Mellin transform [37], defined by $\mathcal{M}^{-1}\{F(\phi), z\} = \frac{1}{2\pi i} \int_{c-i\infty}^{c+i\infty} F(\phi)z^{-\phi} d\phi$, to Eq. (10) yields a set of functions which can be represented by Meijer G-functions as

$$\begin{aligned}
 G_1(z) &= \frac{1}{2\pi i} \int_L F_1(\phi)z^{-\phi} d\phi \stackrel{\text{def}}{=} G_{0,4}^{2,0} \left(\beta_0, \beta_1, \beta_2, \beta_3 \mid z \right), G_2(z) = \frac{1}{2\pi i} \int_L F_2(\phi)z^{-\phi} d\phi \stackrel{\text{def}}{=} G_{0,4}^{4,0} \left(\beta_0, \beta_1, \beta_2, \beta_3 \mid z \right), \\
 G_3(z) &= \frac{1}{2\pi i} \int_L F_3(\phi)z^{-\phi} d\phi \stackrel{\text{def}}{=} G_{0,4}^{2,0} \left(\beta_0, \beta_1, \beta_2, \beta_3 \mid z \right), G_4(z) = \frac{1}{2\pi i} \int_L F_4(\phi)z^{-\phi} d\phi \stackrel{\text{def}}{=} G_{0,4}^{2,0} \left(\beta_0, \beta_2, \beta_1, \beta_3 \mid z \right), \\
 G_5(z) &= \frac{1}{2\pi i} \int_L F_5(\phi)z^{-\phi} d\phi \stackrel{\text{def}}{=} G_{0,4}^{2,0} \left(\beta_0, \beta_3, \beta_1, \beta_2 \mid z \right), G_6(z) = \frac{1}{2\pi i} \int_L F_6(\phi)z^{-\phi} d\phi \stackrel{\text{def}}{=} G_{0,4}^{2,0} \left(\beta_1, \beta_2, \beta_0, \beta_3 \mid z \right), \\
 G_7(z) &= \frac{1}{2\pi i} \int_L F_7(\phi)z^{-\phi} d\phi \stackrel{\text{def}}{=} G_{0,4}^{2,0} \left(\beta_1, \beta_3, \beta_0, \beta_2 \mid z \right), G_8(z) = \frac{1}{2\pi i} \int_L F_8(\phi)z^{-\phi} d\phi \stackrel{\text{def}}{=} G_{0,4}^{2,0} \left(\beta_2, \beta_3, \beta_0, \beta_1 \mid z \right),
 \end{aligned} \tag{11}$$

where i is the imaginary unit, and the Meijer G-functions are defined via a line integral in the complex plane as [36–39]:

$$G_{p,q}^{l,n} \left(\begin{matrix} a_1, \dots, a_p \\ b_1, \dots, b_q \end{matrix} \mid z \right) \stackrel{\text{def}}{=} \frac{1}{2\pi i} \int_L \frac{\prod_{j=1}^l \Gamma(b_j + s) \prod_{j=1}^n \Gamma(1 - a_j - s)}{\prod_{j=1}^p \Gamma(a_j + s) \prod_{j=1}^q \Gamma(1 - b_j - s)} z^{-s} ds, \tag{12}$$

where $a_1 \dots a_p, a_{n+1} \dots a_p, b_1 \dots b_b$, and $b_{l+1} \dots b_q$ are parameter groups. Clearly, a fourth-order differential equation will have four linearly independent solutions. The linear dependence of the functions $\mathcal{S}_{1-8}(z)$ are investigated as follows. If no pair among $\beta_i, i = 0, 1, 2, 3$ differ by an integer, then the four linearly independent solutions are referred to as the fundamental solutions [38]. Exceptional cases in which any pair among β_i differs by an integer are studied in Section 2.2 and the related solutions are called alternative solutions.

Among the solutions of $G_{1-8}(z), G_1(z) = 0$ by Cauchy’s theorem because $F_1(\phi)$ has no poles. $G_{2-8}(z)$ can be represented by a linear combination of another set of Meijer-G functions:

$$\begin{aligned}
 G_2(z) &= a_1 W_0(z) + a_2 W_1(z) + a_3 W_2(z) + a_4 W_3(z), \\
 G_3(z) &= a_5 W_0(z) + a_6 W_1(z), G_4(z) = a_7 W_0(z) + a_8 W_2(z), \\
 G_5(z) &= a_9 W_0(z) + a_{10} W_3(z), G_6(z) = a_{11} W_1(z) + a_{12} W_2(z), \\
 G_7(z) &= a_{13} W_1(z) + a_{14} W_3(z), G_8(z) = a_{15} W_2(z) + a_{16} W_3(z),
 \end{aligned} \tag{13}$$

where $a_1 - 16$ are constants (with detailed derivation shown in Appendix B) and

$$\begin{aligned}
 W_0(z) &= G_{0,4}^{1,0} \left(\beta_0, \beta_1, \beta_2, \beta_3 \mid -z \right), W_1(z) = G_{0,4}^{1,0} \left(\beta_1, \beta_0, \beta_2, \beta_3 \mid -z \right), \\
 W_2(z) &= G_{0,4}^{1,0} \left(\beta_2, \beta_0, \beta_1, \beta_3 \mid -z \right), W_3(z) = G_{0,4}^{1,0} \left(\beta_3, \beta_0, \beta_1, \beta_2 \mid -z \right).
 \end{aligned} \tag{14}$$

Thus, the set of fundamental solutions are given by

$$W(z) = c_0 W_0(z) + c_1 W_1(z) + c_2 W_2(z) + c_3 W_3(z), \tag{15}$$

where $c_0 - 3$ are unknown constants to be determined by boundary and load conditions. As mentioned above, the set of fundamental solutions is valid only if no pairs among β_i differ by an integer, otherwise pairs among $W_i(z)$ will be linearly related. Details are given in the next section.

2.2. Property of linear dependence and alternative solutions among $W_0 - 3$ under different integer difference conditions

To study the linear dependence property among the fundamental solutions, we apply the property of the gamma function of Eq. (9). It is easy to prove that

$$\frac{\Gamma(\beta_i + \phi)}{\Gamma(1 - \beta_j - \phi)} = (-1)^Z \frac{\Gamma(\beta_j + \phi)}{\Gamma(1 - \beta_i - \phi)}, \text{ if } \beta_i - \beta_j = Z \in \mathbb{Z}, i \neq j, \tag{16}$$

where \mathbb{Z} is the set of integers. As a result, we have a pair of linearly dependent solutions

$$W_i(x) = (-1)^Z W_j(x), \tag{17}$$

with the integer difference condition (IDC) of parameters β_i ($i = 0, 1, 2, 3$) of W_{0-3} in Eq. (14)

$$\Delta\beta_{ij} = \beta_i - \beta_j = Z \in \mathbb{Z}, i < j. \tag{18}$$

This means that every two solutions out of the four are linearly dependent if $\Delta\beta_{ij}$ is an integer, thus requiring one alternative solution [36]. $i < j$ is assumed without loss of generality. Since β_i is determined by the exponent m , we derive the corresponding requirements on m from Eq. (18). Obviously, two pairs of $\Delta\beta_{ij}$ are equivalent, namely

$$\Delta\beta_{01} = \Delta\beta_{23}, \Delta\beta_{02} = \Delta\beta_{13}, \tag{19}$$

there are therefore four $\Delta\beta_{ij}$ cases that should be studied, i.e. $\Delta\beta_{01}$, $\Delta\beta_{02}$, $\Delta\beta_{03}$, and $\Delta\beta_{12}$. To illustrate the procedure, we here take the case of $\Delta\beta_{12}$ as an example.

Clearly, satisfying IDC of $\Delta\beta_{12}$ and $m > 2$ requires

$$\begin{cases} \Delta\beta_{12} = \frac{3m-1}{4-2m} = Z \in \mathbb{Z}, \\ m > 2 \end{cases}, \tag{20}$$

which yields the IDC of $\Delta\beta_{12}$ in terms of m as

$$m = \frac{4Z_2 + 3}{2Z_2 - 1}, Z_2 = 1, 2, 3, \dots, \tag{21}$$

which means that $W_1(z)$ and $W_2(z)$ are linearly dependent and therefore alternative solutions are necessary. Recalling Eq. (11), $G_6(z)$ cannot be represented by the linear combination of $W_1(z)$ and $W_2(z)$ because of $\Delta\beta_{12}$ being integer [38]. Thus $G_6(z)$ becomes linearly independent of the fundamental solutions, suitable to be used as an alternative solution:

$$\widehat{W}_1(z) = G_6(z), \tag{22}$$

where ' $\widehat{W}_i(z)$ ' or ' $\widetilde{W}_i(z)$ ' indicate that the solution $W_i(z)$ is replaced by an alternative $\widehat{W}_i(z)$ or $\widetilde{W}_i(z)$. This concludes the case. Alternative solutions in other cases can be obtained based on the same principle.

After investigating all possible $\Delta\beta_{ij}$ cases, we classify all six cases, including the five cases where alternative solutions are required and one case where fundamental solutions, Eq. (15), are available, show the processing routes in Fig. 2, and tabulate the final set of solutions in Table 1.

Obviously, the variable substitution of Eq. (4) is not valid for Case 1 with $m = 2$, which therefore should be treated separately. For

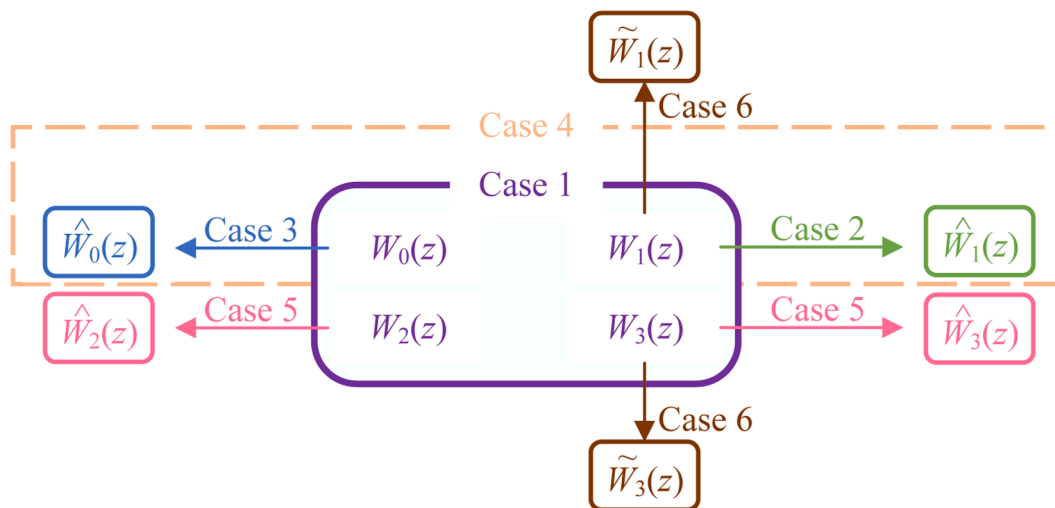


Fig. 2. Classification diagram of alternative solutions of Cases 1-6.

Table 1
Alternative solutions and integer difference condition (IDC) for m in all cases.

	IDC for m	Alternative solutions
Case 1	Complementary set of Cases 2-5	Fundamental solutions, Eq. (15)
Case 2	$m = \frac{4Z_2 + 3}{2Z_2 - 1}, m \neq \frac{4Z_2 + 1}{2Z_2 - 1}, Z_2 = 1, 2, 3, \dots$	$\widehat{W}_1(z) = G_6(z)$
Case 3	$m = \frac{4Z_3 + 1}{2Z_3 - 1}, m \neq \frac{4Z_3 + 3}{2Z_3 - 1}, Z_3 = 1, 2, 3, \dots$	$\widehat{W}_0(z) = G_5(z)$
Case 4	$m = \frac{4Z_4 + 5}{2Z_4 + 1}, Z_4 = 1, 4, 7, \dots$	$\widehat{W}_0(z) = G_5(z)$ $\widehat{W}_1(z) = G_6(z)$
Case 5	$m = \frac{4Z_5 + 2}{2Z_5 - 1}, Z_5 = 1, 2, 3, \dots$	$\widehat{W}_2(z) = G_4(z)$ $\widehat{W}_3(z) = G_7(z)$
Case 6	$m = -\frac{4Z_6 + 1}{2Z_6}, Z_6 = 1, 2, 3, \dots$	$\widehat{W}_1(z) = G_3(z)$ $\widehat{W}_3(z) = G_8(z)$

completeness, a brief derivation is given below.

When $m = 2$, we perform a variable substitution as

$$z = \ln x. \tag{23}$$

This transforms the ODE with variable coefficient into an ODE with constant coefficient which can be easily solved. Appendix C exhibits the process. The solution writes

$$W(x) = x^{-\frac{3}{2}}[c_0 \cos(k_1 \ln x) + c_1 \sin(k_1 \ln x) + c_2 \cosh(k_2 \ln x) + c_3 \sinh(k_2 \ln x)], \tag{24}$$

where

$$k_1 = \sqrt{-\frac{17}{4} + \sqrt{\xi + 4}}, \quad k_2 = \sqrt{\frac{17}{4} + \sqrt{\xi + 4}}. \tag{25}$$

In summary, for any given $m \geq 2$, exact solutions of the flexural wave equation for ABH beam are now all derived. These exact solutions will be applied to derive the dynamic stiffness (DS) matrix, as discussed in Section 2.3 hereafter.

2.3. Derivation of dynamic stiffness matrix using exact solutions

For a given m , the exact fundamental solutions and alternative solutions determined above can be used to construct the DS matrix of an ABH element as follows.

The sign convention for an ABH beam element is defined in Fig. 3. The amplitudes of the angle of rotation Θ , the shear force V , and the bending moment M take the following form

$$\Theta(x) = \frac{dW}{dx}, \tag{26}$$

$$M(x) = EI(x) \frac{d^2W}{dx^2}, \tag{27}$$

$$V(x) = -\frac{d}{dx} \left(EI(x) \frac{d^2W}{dx^2} \right). \tag{28}$$

Referring to Fig. 3, the end conditions for deflections and forces of the beam element can be applied as follows:

$$\begin{aligned} W_1 &= W(x = x_1), \Theta_1 = \Theta(x = x_1), M_1 = -M(x = x_1), V_1 = -V(x = x_1), \\ W_2 &= W(x = x_2), \Theta_2 = \Theta(x = x_2), M_2 = M(x = x_2), V_2 = V(x = x_2). \end{aligned} \tag{29}$$

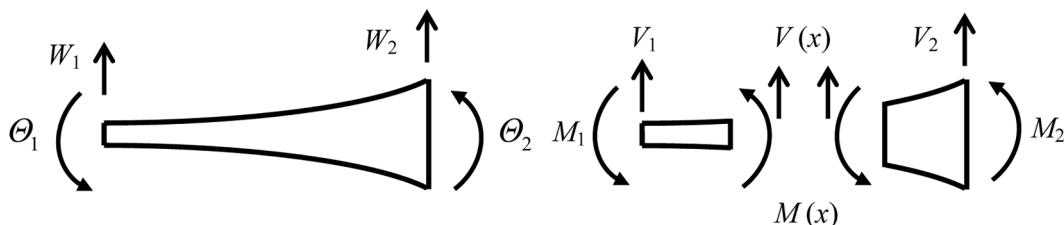


Fig. 3. Sign convention for an ABH beam element.

Substituting Eqs. (12, 28–30) into Eqs. (29) gives

$$\mathbf{d} = \mathbf{D}\bar{\mathbf{c}}, \quad \mathbf{f} = \mathbf{F}\bar{\mathbf{c}}, \tag{30}$$

with

$$\mathbf{d} = \begin{bmatrix} W_1 \\ \Theta_1 \\ W_2 \\ \Theta_2 \end{bmatrix}, \quad \mathbf{f} = \begin{bmatrix} V_1 \\ M_1 \\ V_2 \\ M_2 \end{bmatrix}, \quad \bar{\mathbf{c}} = \begin{bmatrix} c_0 \\ c_1 \\ c_2 \\ c_3 \end{bmatrix}. \tag{31}$$

Eliminating the unknown constant vector $\bar{\mathbf{c}}$ from Eqs. (30) yields the relationship between the force vector and the deflection vector

$$\mathbf{f} = \mathbf{F}\mathbf{D}^{-1}\mathbf{d} = \mathbf{K}\mathbf{d}, \tag{32}$$

and the 4×4 DS matrix \mathbf{K} of the ABH beam can be obtained as

$$\mathbf{K} = \mathbf{F}\mathbf{D}^{-1}. \tag{33}$$

Since there are six different forms of the exact solutions including the alternative solution and it is difficult to simplify the operation of Meijer G-functions, the expressions of \mathbf{K} for all cases are not detailed here. One may obtain them through symbolic operation in a rather straightforward way.

Note that the selection of the coordinate system used in this paper is part of the tactic in order to get the mathematical solution since $h(x)$ expression significantly affects the form of the differential equation when deriving exact solutions. Having said that, the DS matrix established above for ABH beams can be combined with other DS models to analyze compound structures using the same coordinate transformation and assembly procedures as those used in FEM. Characterizations of the dynamics of ABH beams and their assemblies in other coordinate systems are therefore possible using the proposed method. The detailed process of coordinate transformation and element assembly is provided in [30].

3. Numerical procedures, results, and discussions

For steady-state response analysis under a harmonic excitation, the deflection amplitude of the beam ends can be obtained directly via Eq. (32). After obtaining the constant vector, the entire displacement field of the beam can be determined.

A reliable and accurate method, referred to as the Wittrick-Williams (WW) algorithm, was developed [40] for calculating the natural frequencies of structures modeled by DSM. The algorithm, after a trial frequency ω^* is input, directly calculates the number $J(\omega^*)$ of natural frequencies lower than ω^* . A frequency sweep of ω^* will yields the interval where $J(\omega^*)$ undergoes sudden changes, and then the bisection method or other root-finding methods can be applied to compute the natural frequency of any desired order with a preset precision. $J(\omega^*)$ of a structure modelled by DS elements under given boundary conditions can be mathematically expressed as [40]

$$J(\omega^*) = J_0(\omega^*) + s\left(\mathbf{K}_g^\Delta(\omega^*)\right), \tag{34}$$

and

$$J_0(\omega^*) = \sum j_0(\omega^*), \tag{35}$$

where $\mathbf{K}_g^\Delta(\omega^*)$ is the upper triangular matrix applying the Gauss elimination to the global DSM $\mathbf{K}_g(\omega^*)$ after applying boundary condition; function $s(\cdot)$ is the number of negative elements on the leading diagonal of \mathbf{K}_g^Δ ; and $J_0(\omega^*)$ the number of natural frequencies of fully clamped structures lower than ω^* , which is the summation of each $j_0(\omega^*)$, the number of resonant frequencies of every fully clamped component DS elements lower than ω^* .

3.1. Improved WW algorithm for ABH beams

In practice, although $s\left(\mathbf{K}_g^\Delta(\omega^*)\right)$ can be easily obtained, expressions for $j_0(\omega^*)$ can be a problem. In mathematics, it represents the number of zeros of the common denominator δ of the DS matrix below ω^* . Therefore, in an ideal situation where the zeros of δ can be easily solved, j_0 can be analytically expressed, exemplified by the case of uniform rods and beams [40,41]. However, j_0 cannot be directly solved for ABH beams where the common denominator of the DS matrix is expressed by special functions, which accordingly is called the j_0 problem/count [27,41]. To address the j_0 problem for non-uniform beams, a j_0 table approach [31] was developed inspired by the work in [27]. However, the j_0 table approach suffers from the non-convergence problem in the context of ABH beams due to the significant difference between the minimum and the maximum cross-sectional parameters. We therefore need to revamp the approach as detailed below.

To overcome the deficiency of the j_0 table approach for non-uniform beams in previous work which fails in ABH structures because of the significant differences between the minimum and the maximum cross-section parameters, we introduce a reference beam as the

initial guess. The concerned ABH beams are divided into enough segments of stepped beams, each with slightly lower bending stiffness and linear density compared to the original ABH beams. Therefore, the clamped-clamped natural frequencies of the stepped beam and the concerned ABH beam should satisfy

$$\omega_m < \omega_n < \omega_{l(n+1)}, n = 1, 2, 3, \dots, \quad (36)$$

where ω_n is the unknown and n -th resonant frequencies of the clamped-clamped interested beam; ω_m is the n -th resonant frequencies of the clamped-clamped reference beam. ω_m is calculated using WW algorithm for uniform beam assemblies [26,40] without difficulty and a frequency sequence of the reference beam, $\omega_{l1}, \omega_{l2}, \dots, \omega_{lm}, \dots$ serves as stored data. For a given trial frequency ω^* , the position i in the frequency sequence can be determined, satisfying the inequality

$$\omega_{ii} < \omega^* < \omega_{l(i+1)}. \quad (37)$$

Then the newly developed $j_0(\omega^*)$ count is solved and expressed as

$$j_0(\omega^*) = i - \frac{1}{2} [\mathbf{sign}(\delta_l(\omega^*)\delta_l(\omega_{ii})) + 1], \quad (38)$$

where $\mathbf{sign}(\cdot)$ is the sign function and $\delta_l(\omega)$ is the common denominator of the DS matrix of ABH beam, i.e. the determinant of **D** in Eq. (30).

Note that the step beam is not an approximate treatment of ABH beams. The frequency sequence of the stepped beam is not to replace the natural frequencies of ABH beams. Instead, the sequence only serves as stored data to obtain the j_0 count so that WW algorithm can be deployed. Above algorithm still ensures the accuracy and efficiency because the DS matrix **K** in Eq. (35) of ABH beams and its common denominator δ_l in Eq. (38) are derived from the exact shape function. The revamped WW algorithm is applicable to ABH elements, beam assemblies composed of ABH elements, non-uniform DS elements, or any other DS elements where the exact shape functions are represented by special functions. In numerical examples to be discussed in subsequent sections, we apply this revamped algorithm to determine the natural frequencies of ABH beams, demonstrate and verify its extreme accuracy and efficiency.

3.2. Validation of the dynamic stiffness model

In the following-up numerical analyses, steel is used in all examples with elastic modulus $E = 200\text{Gpa}$ and mass density $\rho = 7850\text{kg/m}^3$. The geometrical parameters and boundary conditions are given in tables and figures in due course. FEM simulations are performed using COMSOL Multiphysics, where the Bernoulli-Euler beam theory and the cubic Lagrange elements are employed. The element type of FEM is specified so that readers can reproduce the results. The Meijer G-functions can be evaluated by the built-in functions in mathematical software. Numerical calculations of each entry of the DS matrix are performed with any prescribed precision to ensure the calculation accuracy. The frequency range covered by analysis is chosen to satisfy the inequality $k(x)h(x) \ll 1$ so that shear effects can be neglected, where $k(x)$ is the local flexural wavenumber [35]. For the revamped WW algorithm, stepped uniform beams with 100 segments are used as the reference beam. To challenge proposed method and verify its accuracy, we deliberately selected extreme numerical parameters (a beam with extremely thin residual thickness at the end), thus leading to pronounced variations in wavelengths and wave amplitudes. Relevant to practical realizations, previous studies [42] have shown that a digital controlled virtual ABH can be designed as long as the mechanical impedance of the ABH portion can be predicted using a numerical model and reproduced by a digitally control electro-mechanical element (such as piezoelectric patches). This would allow for avoiding the direct use of the physical ABH as well as avoiding the potential mechanical problems. In that sense, the present model calculation method will be extremely useful. Additionally, normal numerical parameters are considered for application in mechanical engineering.

We first validate the DSM model for Case 1 using $m = 4$, serving as an illustrative example which does not require alternative solutions. An ABH beam is clamped at x_2 and free at x_1 , as shown in Fig. 1. Geometrical parameters of the beam are listed in Table 2. The first fifty natural frequencies are determined using the present method and compared with the FEM results using different numbers of elements (NOE). For conciseness, we choose eight representative values among the first fifty calculated frequencies and presented them in Table 3. All results bear the first five significant figures, and their relative errors (RE) are calculated based on the convergent results of the FEM. The efficiency of the present method can be quantified by showing the NOE used in FEM when calculating natural frequencies of given orders to meet the RE requirements. For instance, at least 43 elements are required for the FEM to give the first 12th natural frequencies to meet 0.1 % RE compared with DSM; 90 and 214 elements are needed for the first 24th natural frequencies to reach a RE below 0.1 % and 0, respectively; etc. Table 3 shows that FEM with insufficient NOE always overestimates the accurate resonant frequencies given by the DSM, which is reasonable. Note that the DSM requires only one element to obtain convergent and accurate results, which otherwise would require significantly large NOE in FEM. The line chart in Fig. 4 is drawn to show the accuracy of the DSM more clearly. The horizontal axis contains five modal orders, while the vertical axis represents the NOE. The blue line

Table 2
Geometrical parameters used in Table 3.

Thickness	$h(x)=0.024x^4, 0.1 \leq x \leq 0.2$
Width	$3.84 \times 10^{-5} \text{ m}$

Table 3
Natural frequencies (Hz) and relative error (values in %) between the two methods.

Mode	FEM (NOE)					DSM (NOE)	
	43	110	90	214	195	981	1
1	3.1463(0)	3.1463(0)	3.1463(0)	3.1463(0)	3.1463(0)	3.1463	3.1463(0)
6	70.586(0.01 %)	70.581(0)	70.582(0)	70.581(0)	70.581(0)	70.581	70.581(0)
12	295.19(0.11 %)	294.89(0)	294.90(0.1 %)	294.88(0)	294.88(0)	294.88	294.88(0)
...							
23	1130.1(1.20 %)	1117.2(0.04 %)	1117.7(0.09 %)	1116.8(0 %)	1116.8(0 %)	1116.8	1116.7(0.01 %)
24	1237.5(1.62 %)	1218.4(0.05 %)	1219.0(0.10 %)	1217.8(0)	1217.9(0.01 %)	1217.8	1217.8(0)
...							
48	5800.7(16.9 %)	4993.6(0.64 %)	5027.0(1.31 %)	4964.7(0.05 %)	4965.9(0.08 %)	4962.0	4962.0(0)
49	6053.8(17.0 %)	5208.2(0.68 %)	5251.9(1.53 %)	5176.0(0.06 %)	5177.3(0.09 %)	5172.9	5172.9(0)
50	6393.8(18.7 %)	5427.4(0.73 %)	5485.6(1.81 %)	5391.7(0.06 %)	5393.2(0.09 %)	5388.2	5388.2(0)

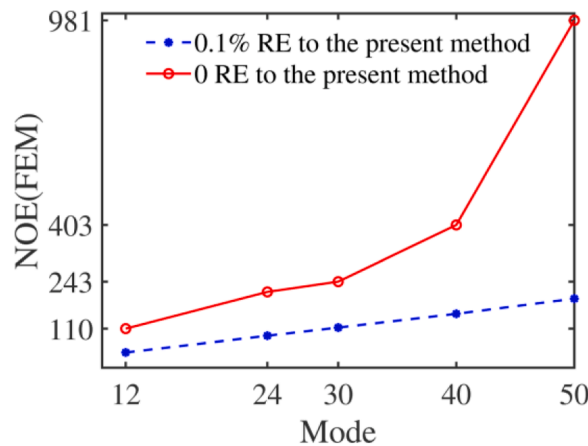


Fig. 4. NOE used in FEM to calculate fifty natural frequencies to meet the RE requirement.

represents the NOE required to calculate fifty resonant frequencies and meet 0.1 % RE requirement. The red line represents the NOE to calculate fifty resonant frequencies and meet 0 RE requirement. To accurately handle higher order modes, the NOE required in the finite element method undergoes a sharp increase (red line).

To further test the accuracy of the proposed method, two additional ABH beam configurations are analyzed by choosing more realistic beam dimensions (to accommodate practical fabrication requirement). Configuration 1 follows a thickness profile of $h(x) = 0.016x^4$ with $0.5 \leq x \leq 0.9$ and Configuration 2 has $h(x) = 0.0256x^4$ with $0.75 \leq x \leq 0.95$. Note both configurations share identical tip thicknesses $h_1 = 1$ mm and widths $b = 2$ cm. Both ABH beams are clamped at x_2 and free at x_1 , as illustrated in Fig. 1. The first 50 natural frequencies of flexure modes are computed using the present method and FEM with different number of elements. The results show good agreement between the two approaches, with a few representative and arbitrarily selected data tabulated in Table 4 for illustration purposes.

Then a uniform beam whose thickness is the same as ABH at x_2 is attached to the ABH, as shown in Fig. 5. A harmonic force $f(t)$ with an amplitude of $F_0 = 1$ N is applied at x_f . Geometrical parameters are listed in Table 5. The end node x_3 is clamped and other nodes are free. The frequency response functions (FRF) are calculated using FEM and DSM, respectively. Two configurations of NOE (300, 500) used in FEM are considered. Only three elements, i.e. one ABH beam element and two uniform beam elements are used in the DSM.

Table 4
Natural frequencies (Hz) of two configurations in mechanical background.

Mode number		Method (NOE)	1	2	3	8	12	20	40	50
Configuration 1	FEM (100)		56.088	162.17	352.99	2677.1	6201.0	17700	72652	$1.1455 \cdot 10^5$
	FEM (200)		56.088	162.17	352.99	2677.1	6200.8	17696	72407	$1.1371 \cdot 10^5$
	FEM (500)		56.088	162.17	352.99	2677.1	6200.8	17696	72388	$1.1364 \cdot 10^5$
	DSM (1)		56.088	162.17	352.99	2677.1	6200.8	17696	72388	$1.1364 \cdot 10^5$
Configuration 2	FEM (100)		457.56	1982.8	4980.1	42178	98696	$2.8315 \cdot 10^5$	$1.1628 \cdot 10^6$	$1.8304 \cdot 10^6$
	FEM (200)		457.56	1982.8	4980.1	42178	98696	$2.8312 \cdot 10^5$	$1.1607 \cdot 10^6$	$1.8230 \cdot 10^6$
	FEM (500)		457.56	1982.8	4980.1	42178	98696	$2.8312 \cdot 10^5$	$1.1606 \cdot 10^6$	$1.8225 \cdot 10^6$
	DSM (1)		457.56	1982.8	4980.2	42178	98696	$2.8312 \cdot 10^5$	$1.1606 \cdot 10^6$	$1.8224 \cdot 10^6$
	DSM (500)		457.56	1982.8	4980.2	42178	98696	$2.8312 \cdot 10^5$	$1.1606 \cdot 10^6$	$1.8224 \cdot 10^6$

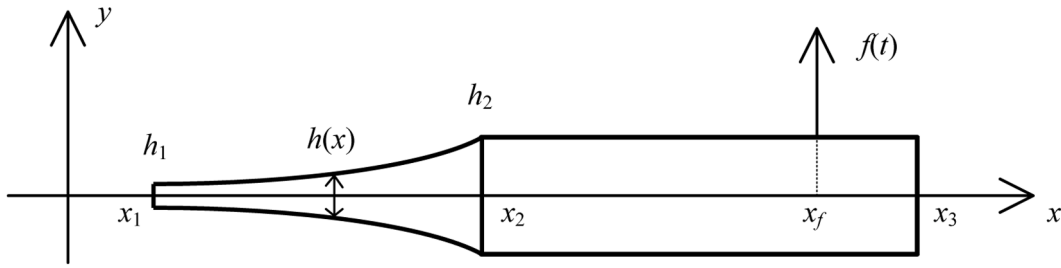


Fig. 5. An ABH beam attached to a uniform beam is excited by a harmonic point force $f(t)$.

Table 5
Geometrical parameters used in Fig. 6.

Thickness of ABH	$h(x)=0.024x^4, 0.1 \leq x \leq 0.2$
Thickness of the uniform beam	3.84×10^{-5} m
Coordinate range of the uniform beam	$0.2 \leq x \leq 1/3$
Point of application of $f(t)$	$x_f = 0.3$ m
Response point	x_1 in Fig. 5 (tip)
Width	3.84×10^{-5} m

Results in the low frequency range (0-500 Hz) and higher frequency range (4000-5000 Hz) are shown in Fig. 6(a) and Fig. 6(b), respectively, which both show good agreement between the DSM and FEM using sufficient (500) NOE. As the NOE used in FEM increases, the FEM results converge towards those from the DSM.

The DSM models for Cases 2-6 are also validated in terms of FRF analysis through comparison with FEM using 500 NOE. Since Case 4 is a combination of Cases 2 and 3, only Cases 4, 5, and 6 are presented here by choosing m as 3, 2.8, and 2.5, respectively. The case with $m = 2$ is also included in the comparison for the completeness of the validation. Geometrical parameters used in the calculations are given in Table 6. Note other parameters remain the same among different cases. Fig. 7(a-d) show the FRF curves of the four structures in 0-1000 Hz, all showing good agreement between the two sets of results.

To examine the ability of DSM in characterizing typical ABH phenomena, Fig. 8(a-d) show the displacement amplitudes of the structure described by Fig. 5 and Table 6 and subjected to the same harmonic point force excitation at an arbitrarily selected frequency $f = 240$ Hz. Again, only one ABH element is used in the DSM to obtain the whole displacement field of the ABH beam. From the plotted deformation shapes, one can see the typical ABH phenomena: progressively shortened local wavelengths, increased oscillating amplitudes along the decreased structural thickness, and increasing energy concentration near the ABH tip. One can also observe that at the same frequency, more pronounced ABH phenomena occur in the structures with a larger m , when all other ABH parameters remain unchanged.

In summary, the proposed DSM models for ABH elements with $m \geq 2$ are systematically validated. Using just one element, DSM can accurately describe the entire displacement field of the ABH and capture the ABH behavior. It can be surmised that more complex structures composed of ABH beams can also be efficiently modeled in the DSM framework due to the versatility of the DSM.

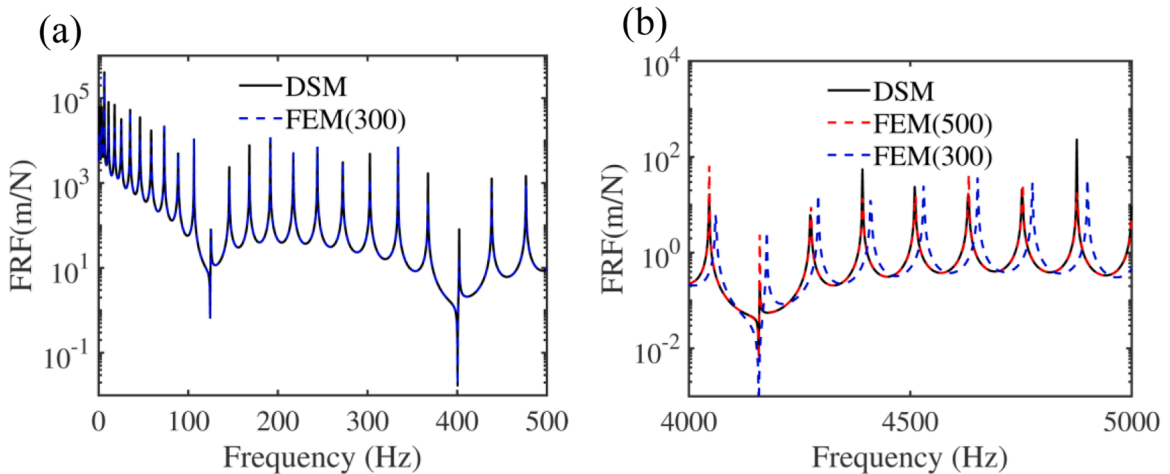


Fig. 6. FRF curves $|w|/F_0$ of ABH with $m = 4$ of Case 1 calculated by DSM and FEM.

Table 6
Geometrical parameters used in Figs. 7 and 8.

m	2, 2.5, 2.8, 3
Thickness of ABH	$h(x)=0.001x^m, 0.2 \leq x \leq 0.4$
Thickness of the uniform beam	$h(0.4)$
Coordinate range of the uniform beam	$0.4 \leq x \leq 0.5$
Point of application of $f(t)$	$x_f = 0.48$ m
Response point	x_1 in Fig. 5 (tip)
Width	0.04 m

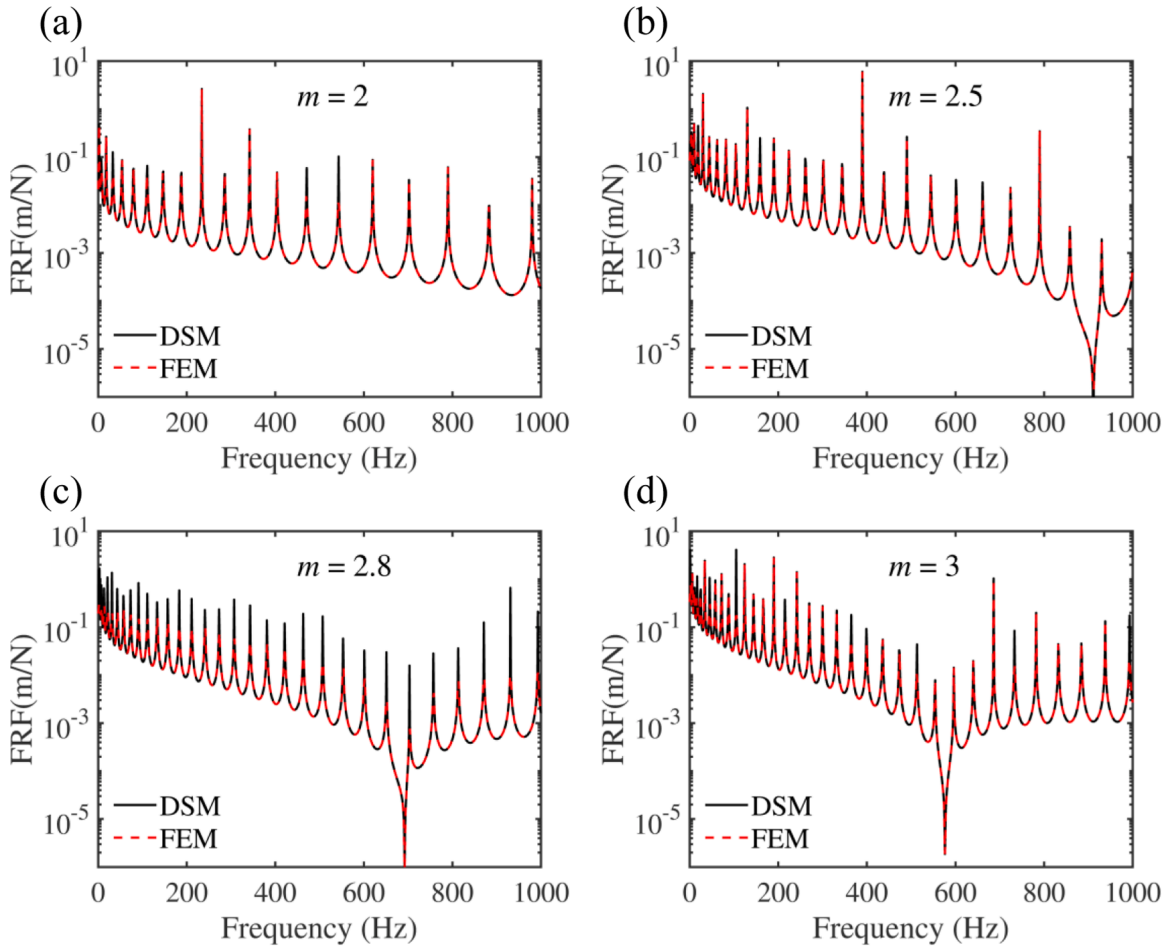


Fig. 7. FRF curves $|w|/F_0$ calculated by DSM and FEM of ABH with: (a) $m = 2$, (b) $m = 2.5$ of Case 6, (c) $m = 2.8$ of Case 5, (d) $m = 3$ of Case 4.

3.3. Comparison of exact solution using Meijer G-function and hypergeometric function [35]

It should be noted that the exact solutions expressed by the hypergeometric function (HGF) [35] may, in principle, also be employed to derive the DS matrix. This option, however, was abandoned due to two reasons. One is that series solutions will inevitably introduce series approximation when using finite terms. Although the HGF has become built-in functions in most mathematical software, the alternative solutions contain other infinite series which cannot avoid approximation, resulting in inaccuracy approximation. Another reason is that alternative solutions and their derivatives with complicated series forms may require considerable computational effort.

To substantiate the above arguments, we present a quantified comparison of two DSM models using respectively the Meijer G-function (DSM-MG) and HGF (DSM-HG) with finite terms N . An ABH beam shown in Fig. 1 and clamped at x_2 is used again for this purpose. Geometrical parameters used are listed in Table 7. The first thirteen natural frequencies have been determined. We examine four representative natural frequencies, namely the 7th, 9th, 11th, and 13th, with results tabulated in Table 8. Three models, including DSM-HG, DSM-MG, and FEM with 500 NOE, are included for comparison. The number of terms of the HGF series taken in DSM-HG is

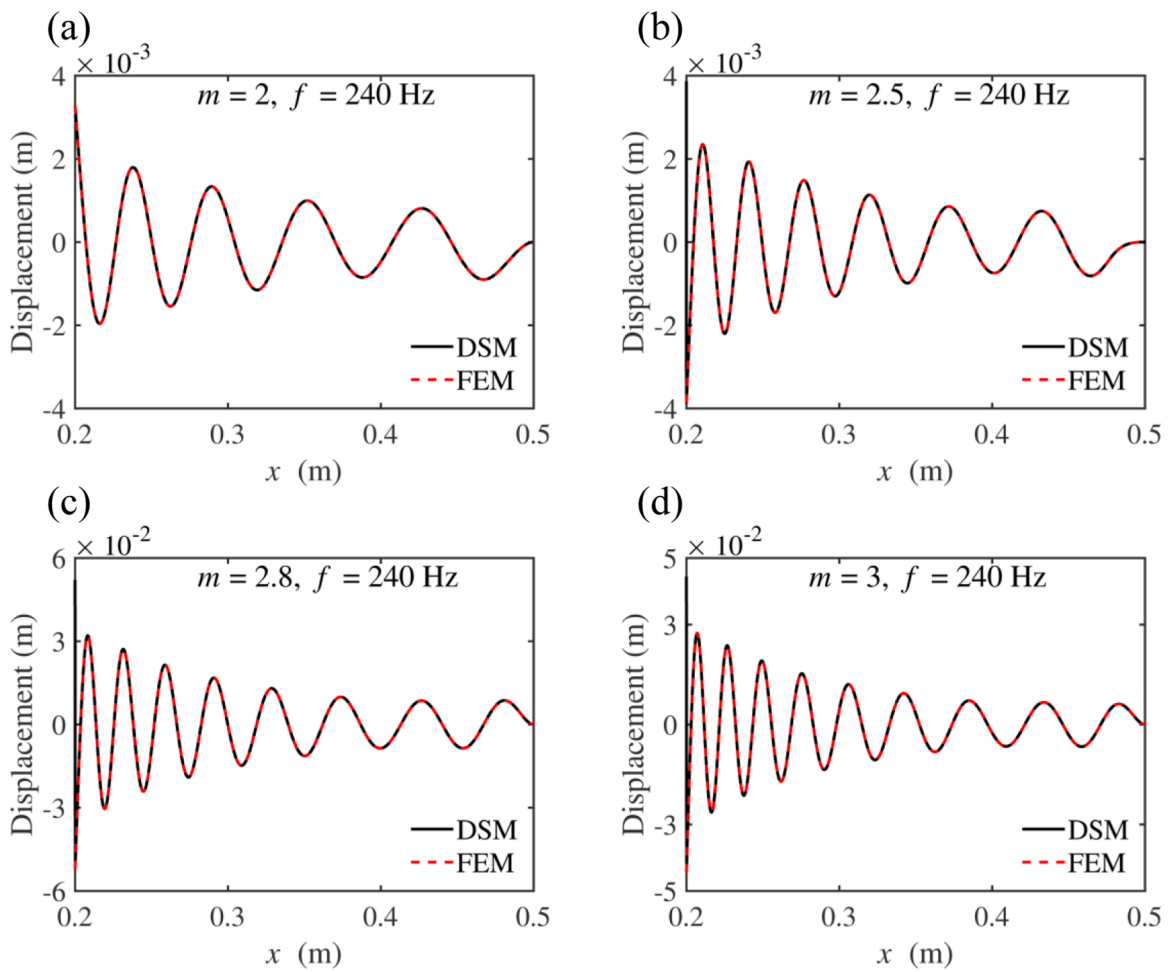


Fig. 8. Displacement amplitude at 240 Hz calculated by DSM and FEM of ABH with: (a) $m = 2$, (b) $m = 2.5$ of Case 6, (c) $m = 2.8$ of Case 5, (d) $m = 3$ of Case 4.

Table 7
Geometrical parameters used in Table 8.

Thickness	$h(x)=0.001x^{2.8}, 0.2 \leq x \leq 0.4$
Width	0.04 m

Table 8
Natural frequencies (Hz) determined by three models. '-' represents that the result does not converge.

Mode	DSM				DSM-MG	FEM
	DSM-HG (number of terms of series taken)					
	80	100	120	150		
7	74.789	74.789	74.789	74.789	74.789	74.789
9	-	126.51	126.51	126.51	126.51	126.51
11	-	-	192.02	192.02	192.02	192.02
13	-	-	-	271.31	271.31	271.31

80, 100, 120, and 150, respectively.

Table 8 shows that a good agreement is reached between DSM-MG and FEM. The convergent 7th and 9th resonant frequencies require 80 and 100 terms, respectively, for DSM-HG. The 11th and 13th resonant frequencies would require 120 and 150 terms, respectively, for DSM-HG to achieve reasonably accurate result. The determinant of the DS matrix of DSM-MG and DSM-HG with

different terms of series taken is plotted in Fig. 9. Each zero point of the determinant represents a natural frequency. It is clear that DSM-HG using finite terms cannot be applied to forecast the determinant accurately. As more terms are used, curves of DSM-HG converge towards those from DSM-MG, which explains the reason behind the inaccurate prediction of the natural frequency using DSM-HG in Table 8. Undoubtedly, higher resonant modes would require more terms to be included in the DSM-HG to reach the desired convergence, at the expenses of increasing computational cost.

We also perform the response analysis by constructing linear equations regarding undetermined coefficients through boundary conditions and continuity conditions (the same procedure as [35]) to clarify the concerns that the application of DSM will not require higher terms of series than classical method in [35]. The structure in Table 6 for the Case $m = 2.8$ is considered and other configurations are the same. The displacement response amplitude of the ABH plotted in Fig. 10 is calculated by applying exact solutions expressed by HGF and Meijer G-functions for comparison. Fig. 10(a–d) clearly show that more terms of HGF are needed in higher frequencies to capture the ABH phenomena, to be on pair with Meijer G-functions.

4. Conclusions

In this paper, the exact shape functions for ABH of arbitrary power $m \geq 2$ are mathematically derived based on the Euler-Bernoulli theory and used to further derive the exact dynamic stiffness matrix through symbolic computation. For $m > 2$, the integral representations of the exact solutions are derived by the application of the Mellin integral transformation and are expressed by the Meijer G-functions. Solution for the special case with $m = 2$ is also derived for providing a complete set of solutions to all ABH-relevant configurations. Considering the requirements for linearly independent solutions, we classify m into six cases depending on the integer difference condition. To accommodate the ABH-specific needs, the Wittrick-Williams algorithm is re-visited and revamped. Numerical examples show that the proposed DSM models, which cover all ABH cases with $m \geq 2$, alongside the improved algorithm, offer high accuracy and efficiency in performing dynamic analysis of ABH beams featuring highly compressed and non-uniformly distributed wavelength. Only one element is needed to capture the typical ABH behavior of an ABH beam. Comparisons between the integral and

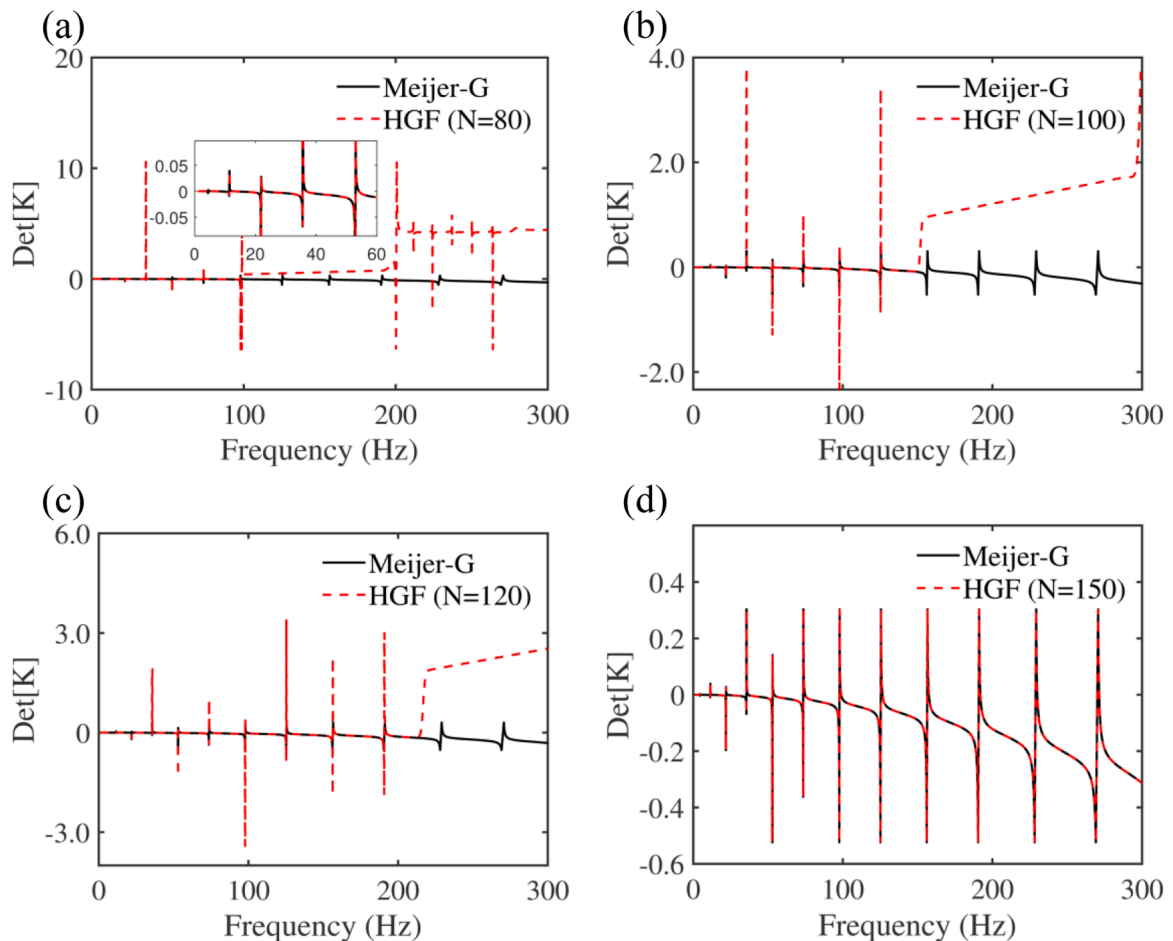


Fig. 9. Determinant of the dynamic stiffness matrix of DSM-MG and DSM-HG with: (a) 80 terms (b) 100 terms (c) 120 terms (d) 150 terms of series taken.

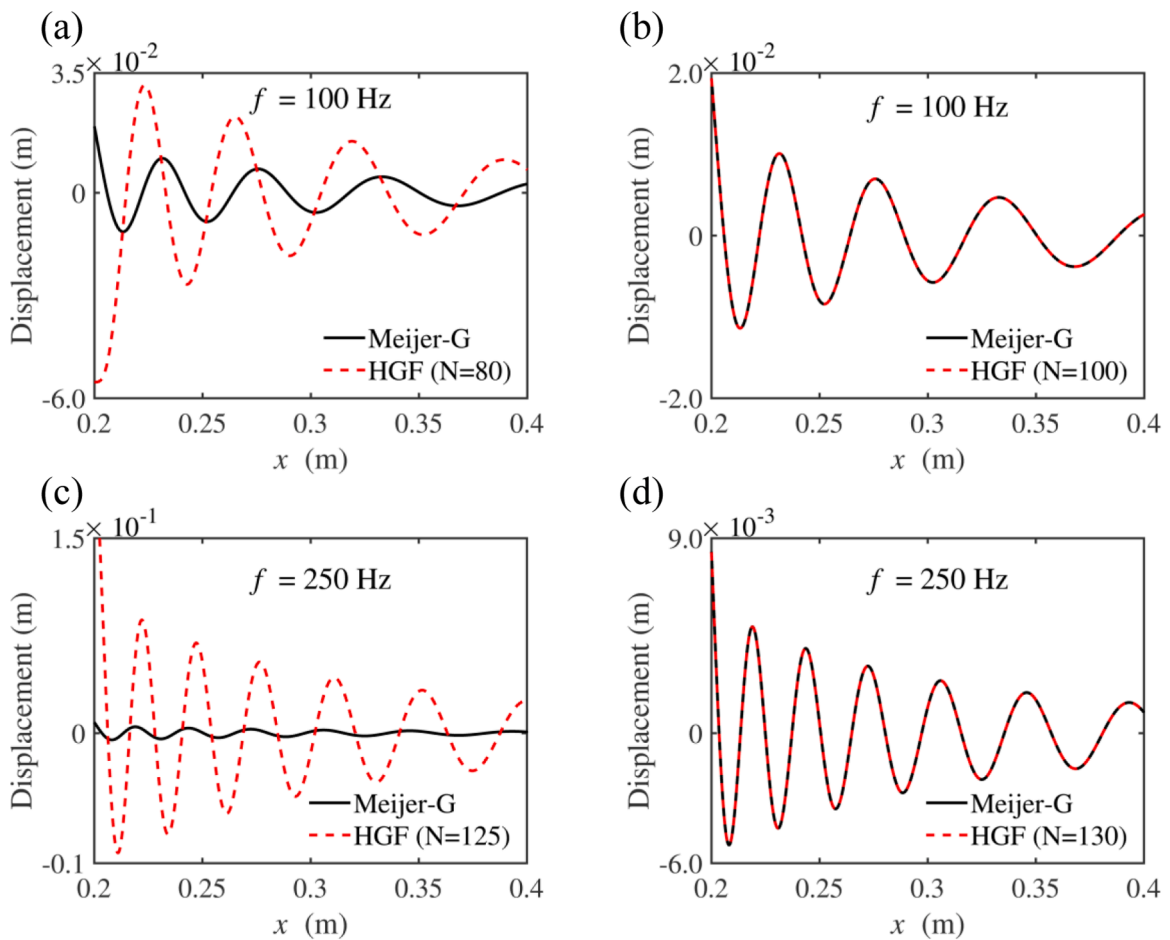


Fig. 10. Displacement amplitude calculated by Meijer G-functions and HGF with: (a) 80 terms at 100 Hz, (b) 100 terms at 100 Hz, (c) 125 terms at 250 Hz, (d) 130 terms at 250 Hz.

series representations of the exact shape functions show the clear advantages of the former in terms of accuracy and efficiency, especially for high frequency calculations.

The present studies offer a full set of accurate solutions to ABH beam modelling, covering all ABH-relevant cases with exponent equal to and larger than 2 (as specified by the smoothness condition imposed by ABH theory). Therefore, the model can be exploited and used to conceive and analyze more complex ABH assemblies which use ABH beams as constituent building elements. For such complex structures, the overwhelming advantages of the proposed method over purely numerical ones such as FEM can be anticipated.

CRediT authorship contribution statement

Le Chang: Writing – review & editing, Writing – original draft, Validation, Methodology, Investigation, Data curation, Conceptualization. **Li Cheng:** Writing – review & editing, Supervision, Project administration, Funding acquisition.

Declaration of competing interest

The authors declare that they have no known competing financial interests or personal relationships that could have appeared to influence the work reported in this paper.

Acknowledgements

We appreciate Dutch mathematician Prof. C. S. Meijer and his collaborators for their contributions to the Meijer G-functions.

Appendix A. Mathematical derivation of the recursion Eq. (8)

Introducing the differential operator $\Theta = z \frac{d}{dz}$ and taking $\beta_0 = 0$ (Eq. (7)), Eq. (6) is rewritten as

$$[\Theta(\Theta - \beta_1)(\Theta - \beta_2)(\Theta - \beta_3) - \psi]W(\psi) = 0, \tag{A.1}$$

which can be further expanded to

$$\Theta^4 W - \Theta^3 W(\beta_1 + \beta_2 + \beta_3) + \Theta^2 W(\beta_1\beta_2 + \beta_1\beta_3 + \beta_2\beta_3) - \Theta W\beta_1\beta_2\beta_3 - zW = 0. \tag{A.2}$$

Here we note

$$\Theta^2 W = z \frac{d}{dz} \left(z \frac{dW}{dz} \right) = z \frac{dW}{dz} + z^2 \frac{d^2 W}{dz^2} \neq z^2 \frac{d^2 W}{dz^2}, \tag{A.3}$$

to avoid oversights. The property of Mellin transform of differential operators and the shifting property [37] writes

$$M\{\Theta^n W(z), \phi\} = (-1)^n \phi^n F(\phi), M\{zW(z), \phi\} = F(\phi + 1). \tag{A.4}$$

Applying these properties to Eq. (A.2) yields

$$\phi^4 F(\phi) + \phi^3 F(\phi)(\beta_1 + \beta_2 + \beta_3) + \phi^2 F(\phi)(\beta_1\beta_2 + \beta_1\beta_3 + \beta_2\beta_3) + \phi F(\phi)\beta_1\beta_2\beta_3 - F(\phi + 1) = 0, \tag{A.5}$$

which can be simplified as Eq. (8), i.e.

$$(\beta_0 + \phi)(\beta_1 + \phi)(\beta_2 + \phi)(\beta_3 + \phi)F(\phi) = F(\phi + 1). \tag{A.6}$$

Appendix B. Proof of the linear relation between $W_{0-3}(z)$ and $G_{1-8}(z)$ expressed by Eq. (13)

The proof of linear relation between $W_{0-3}(z)$ and $G_{1-8}(z)$ can be done by representing $W_{0-3}(z)$ and $G_{1-8}(z)$ in terms of the generalized hypergeometric functions, using [38]:

$$G_{p,q}^{l,n} \left(\begin{matrix} a_p \\ b_q \end{matrix} \middle| z \right) = \sum_{h=1}^l \frac{\prod_{j=1}^l (b_j - b_h)^* \prod_{j=1}^n (1 + b_h - a_j) z^{b_h}}{\prod_{j=1}^q \Gamma(1 + b_h - b_j) \prod_{j=n+1}^p \Gamma(a_j - b_h)} {}_pF_{q-1} \left(\begin{matrix} 1 + b_h - a_p \\ (1 + b_h - b_q)^* \end{matrix} \middle| (-1)^{p-l-n} z \right), \tag{B.1}$$

where $\mathbf{a}_p = \{a_1 \dots a_p\}$, $\mathbf{b}_q = \{b_1 \dots b_p\}$, $(\cdot)^*$ indicates that the terms corresponding to $j=h$ and $q=h$ are omitted, and the generalized hypergeometric functions are defined by a power series:

$${}_pF_q \left(\begin{matrix} \mathbf{a}_p \\ \mathbf{b}_q \end{matrix} \middle| z \right) = \sum_{k=0}^{\infty} \frac{(a_1)_k \dots (a_p)_k}{(b_1)_k \dots (b_q)_k} \frac{z^k}{k!}, \tag{B.2}$$

where $(\cdot)_k$ is the Pochhammer symbol. An example for obtaining a_{1-4} is given below. $G_2(z)$ can be expressed by

$$\begin{aligned} G_2(z) &= G_{0,4}^{4,0}(b_0|z) = \sum_{h=1}^4 \left\{ \prod_{j=1}^4 [\Gamma(\beta_{j-1} - \beta_{h-1})^*] z^{\beta_{h-1}} {}_0F_3((1 + \beta_{h-1} - b_0)^* | (-1)^{-4} z) \right\} \\ &= \Gamma(\beta_1 - \beta_0)\Gamma(\beta_2 - \beta_0)\Gamma(\beta_3 - \beta_0) z^{\beta_0} {}_0F_3(b_1|z) + \Gamma(\beta_0 - \beta_1)\Gamma(\beta_2 - \beta_1)\Gamma(\beta_3 - \beta_1) z^{\beta_1} {}_0F_3(b_2|z) \\ &+ \Gamma(\beta_0 - \beta_2)\Gamma(\beta_1 - \beta_2)\Gamma(\beta_3 - \beta_2) z^{\beta_2} {}_0F_3(b_3|z) + \Gamma(\beta_0 - \beta_3)\Gamma(\beta_1 - \beta_3)\Gamma(\beta_2 - \beta_3) z^{\beta_3} {}_0F_3(b_4|z) \end{aligned} \tag{B.3}$$

where

$$\begin{aligned} \mathbf{b}_0 &= \{\beta_0, \beta_1, \beta_2, \beta_3\}, \\ \mathbf{b}_1 &= \{1 + \beta_0 - \beta_1, 1 + \beta_0 - \beta_2, 1 + \beta_0 - \beta_3\}, \mathbf{b}_2 = \{1 + \beta_1 - \beta_0, 1 + \beta_1 - \beta_2, 1 + \beta_1 - \beta_3\}, \\ \mathbf{b}_3 &= \{1 + \beta_2 - \beta_0, 1 + \beta_2 - \beta_1, 1 + \beta_2 - \beta_3\}, \mathbf{b}_4 = \{1 + \beta_3 - \beta_0, 1 + \beta_3 - \beta_1, 1 + \beta_3 - \beta_2\}. \end{aligned} \tag{B.4}$$

$W_{0-3}(z)$ can be expressed by

$$\begin{aligned}
 W_0(z) &= \frac{1}{\Gamma(1 + \beta_0 - \beta_1)\Gamma(1 + \beta_0 - \beta_2)\Gamma(1 + \beta_0 - \beta_3)} (-1)^{\beta_0} z^{\beta_0} {}_0F_3 \left(\begin{matrix} | \\ \mathbf{b}_1 \end{matrix} \middle| (-1)^{-3} (-z) \right), \\
 W_1(z) &= \frac{1}{\Gamma(1 + \beta_1 - \beta_0)\Gamma(1 + \beta_1 - \beta_2)\Gamma(1 + \beta_1 - \beta_3)} (-1)^{\beta_1} z^{\beta_1} {}_0F_3 \left(\begin{matrix} | \\ \mathbf{b}_2 \end{matrix} \middle| z \right), \\
 W_2(z) &= \frac{1}{\Gamma(1 + \beta_2 - \beta_0)\Gamma(1 + \beta_2 - \beta_1)\Gamma(1 + \beta_2 - \beta_3)} (-1)^{\beta_2} z^{\beta_2} {}_0F_3 \left(\begin{matrix} | \\ \mathbf{b}_3 \end{matrix} \middle| z \right), \\
 W_3(z) &= \frac{1}{\Gamma(1 + \beta_3 - \beta_0)\Gamma(1 + \beta_3 - \beta_1)\Gamma(1 + \beta_3 - \beta_2)} (-1)^{\beta_3} z^{\beta_3} {}_0F_3 \left(\begin{matrix} | \\ \mathbf{b}_4 \end{matrix} \middle| z \right).
 \end{aligned}
 \tag{B.5}$$

It is shown that

$$G_2(z) = a_1 W_0(z) + a_2 W_1(z) + a_3 W_2(z) + a_4 W_3(z), \tag{B.6}$$

where $a_1 - 4$ are constants given by

$$\begin{aligned}
 a_1 &= \frac{\Gamma(1 + \beta_0 - \beta_1)\Gamma(1 + \beta_0 - \beta_2)\Gamma(1 + \beta_0 - \beta_3)(-1)^{-\beta_0}\Gamma(\beta_1 - \beta_0)\Gamma(\beta_2 - \beta_0)\Gamma(\beta_3 - \beta_0)}{(-1)^{-\beta_0} \frac{\pi^3}{\sin\pi(\beta_1 - \beta_0)\sin\pi(\beta_2 - \beta_0)\sin\pi(\beta_3 - \beta_0)}}, \\
 a_2 &= \frac{(-1)^{-\beta_1} \frac{\pi^3}{\sin\pi(\beta_0 - \beta_1)\sin\pi(\beta_2 - \beta_1)\sin\pi(\beta_3 - \beta_1)}}{(-1)^{-\beta_1} \frac{\pi^3}{\sin\pi(\beta_0 - \beta_1)\sin\pi(\beta_2 - \beta_1)\sin\pi(\beta_3 - \beta_1)}}, \\
 a_3 &= \frac{(-1)^{-\beta_2} \frac{\pi^3}{\sin\pi(\beta_0 - \beta_2)\sin\pi(\beta_1 - \beta_2)\sin\pi(\beta_3 - \beta_2)}}{(-1)^{-\beta_2} \frac{\pi^3}{\sin\pi(\beta_0 - \beta_2)\sin\pi(\beta_1 - \beta_2)\sin\pi(\beta_3 - \beta_2)}}, \\
 a_4 &= \frac{(-1)^{-\beta_3} \frac{\pi^3}{\sin\pi(\beta_0 - \beta_3)\sin\pi(\beta_1 - \beta_3)\sin\pi(\beta_2 - \beta_3)}}{(-1)^{-\beta_3} \frac{\pi^3}{\sin\pi(\beta_0 - \beta_3)\sin\pi(\beta_1 - \beta_3)\sin\pi(\beta_2 - \beta_3)}}.
 \end{aligned}
 \tag{B.7}$$

which concludes the case. $a_5 - 16$ can be calculated similarly as

$$\begin{aligned}
 a_5 &= \frac{(-1)^{-\beta_0} \pi}{\sin\pi(\beta_1 - \beta_0)}, a_6 = \frac{(-1)^{-\beta_1} \pi}{\sin\pi(\beta_0 - \beta_1)}, a_7 = \frac{(-1)^{-\beta_0} \pi}{\sin\pi(\beta_2 - \beta_0)}, a_8 = \frac{(-1)^{-\beta_2} \pi}{\sin\pi(\beta_0 - \beta_2)}, \\
 a_9 &= \frac{(-1)^{-\beta_0} \pi}{\sin\pi(\beta_3 - \beta_0)}, a_{10} = \frac{(-1)^{-\beta_3} \pi}{\sin\pi(\beta_0 - \beta_3)}, a_{11} = \frac{(-1)^{-\beta_1} \pi}{\sin\pi(\beta_2 - \beta_1)}, a_{12} = \frac{(-1)^{-\beta_2} \pi}{\sin\pi(\beta_1 - \beta_2)}, \\
 a_{13} &= \frac{(-1)^{-\beta_1} \pi}{\sin\pi(\beta_3 - \beta_1)}, a_{14} = \frac{(-1)^{-\beta_3} \pi}{\sin\pi(\beta_1 - \beta_3)}, a_{15} = \frac{(-1)^{-\beta_2} \pi}{\sin\pi(\beta_3 - \beta_2)}, a_{16} = \frac{(-1)^{-\beta_3} \pi}{\sin\pi(\beta_2 - \beta_3)}.
 \end{aligned}
 \tag{B.8}$$

The above derivation is valid if no pairs among β_i differ by an integer. Thus, the linear dependence between $W_0 - 3(z)$ is discussed in Section 2.2.

Appendix C. Exact solutions for $m=2$

Let $m=2$. Eq. (2) is rewritten as

$$x^4 \frac{d^4 W}{dx^4} + 12x^3 \frac{d^3 W}{dx^3} + 30x^2 \frac{d^2 W}{dx^2} - \xi W(x) = 0, \tag{C.1}$$

where

$$\xi = 12\rho\omega^2/E\varepsilon^2. \tag{C.2}$$

Application of a variable substitution as

$$z = \ln x, \tag{C.3}$$

can transform Eq. (C.1) into

$$\frac{d^4 W}{dz^4} + 6 \frac{d^3 W}{dz^3} + 5 \frac{d^2 W}{dz^2} - 12 \frac{dW}{dz} - \xi W(z) = 0, \tag{C.4}$$

which is a differential equation with constant coefficient. Then we may assume a trial solution in the form $W = e^{\lambda z}$ to obtain the characteristic equation as

$$\lambda^4 + 6\lambda^3 + 5\lambda^2 - 12\lambda - \xi = 0, \quad (\text{C.5})$$

whose roots write

$$\lambda_{1,2} = -\frac{3}{2} \pm ik_1, \lambda_{3,4} = -\frac{3}{2} \pm k_2, \quad (\text{C.6})$$

where

$$k_1 = \sqrt{-\frac{17}{4} + \sqrt{\xi + 4}}, k_2 = \sqrt{\frac{17}{4} + \sqrt{\xi + 4}}. \quad (\text{C.7})$$

Clearly, k_2 is always a real number and k_1 can be either a positive real or an imaginary number, depending on the frequency value. Here we use the trigonometric functions defined in the complex plane, allowing for eliminating the discussion about k_1 , and then the solution can be expressed as

$$W(x) = x^{\frac{3}{2}}[c_0 \cos(k_1 \ln x) + c_1 \sin(k_1 \ln x) + c_2 \cosh(k_2 \ln x) + c_3 \sinh(k_2 \ln x)], \quad (\text{C.8})$$

where $c_0 - c_3$ are unknown constants to be determined by boundary conditions.

Data availability

Data will be made available on request.

References

- [1] M. Mironov, Propagation of a flexural wave in a plate whose thickness decreases smoothly to zero in a finite interval, *Sov. Phys. Acoust.* 34 (1988) 318–319.
- [2] V.V. Krylov, F.J.B.S. Tilman, Acoustic ‘black holes’ for flexural waves as effective vibration dampers, *J. Sound Vib.* 274 (2004) 605–619.
- [3] H. Li, O. Doaré, C. Touzé, A. Pelat, F. Gautier, Energy harvesting efficiency of unimorph piezoelectric acoustic black hole cantilever shunted by resistive and inductive circuits, *Int. J. Solids Struct.* 238 (2022) 111409.
- [4] W. Du, Z. Xiang, X. Qiu, Stochastic analysis of an acoustic black hole piezoelectric energy harvester under Gaussian white noise excitation, *Appl. Math. Model.* 131 (2024) 22–32.
- [5] P. Eberhard, *Calm, Smooth and Smart: Novel Approaches for Influencing Vibrations by Means of Deliberately Introduced Dissipation*, ed., Springer Nature Switzerland, Cham, 2024.
- [6] G. Raybaud, J.Y. Lee, W. Jeon, A. Pelat, F. Gautier, On the control of the absorption of an Acoustic Black Hole by using attached point supports, *J. Sound Vib.* 548 (2023) 117562.
- [7] V.B. Georgiev, J. Cuenca, F. Gautier, L. Simon, V.V. Krylov, Damping of structural vibrations in beams and elliptical plates using the acoustic black hole effect, *J. Sound Vib.* 330 (2011) 2497–2508.
- [8] X. Li, Q. Ding, Analysis on vibration energy concentration of the one-dimensional wedge-shaped acoustic black hole structure, *J. Intell. Mater. Syst. Struct.* 29 (2018) 2137–2148.
- [9] O. Guasch, P. Sánchez-Martín, D. Ghilardi, Application of the transfer matrix approximation for wave propagation in a metafluid representing an acoustic black hole duct termination, *Appl. Math. Model.* 77 (2020) 1881–1893.
- [10] H. Sheng, M.-X. He, X.-F. Lyu, Q. Ding, Ultra-low frequency broadband gap optimization of 1D periodic structure with dual power-law acoustic black holes, *J. Intell. Mater. Syst. Struct.* 33 (2022) 532–546.
- [11] L. Tang, L. Cheng, H. Ji, J. Qiu, Characterization of acoustic black hole effect using a one-dimensional fully-coupled and wavelet-decomposed semi-analytical model, *J. Sound Vib.* 374 (2016) 172–184.
- [12] V. Denis, A. Pelat, F. Gautier, B. Elie, Modal Overlap Factor of a beam with an acoustic black hole termination, *J. Sound Vib.* 333 (2014) 2475–2488.
- [13] V. Denis, F. Gautier, A. Pelat, J. Poittevin, Measurement and modelling of the reflection coefficient of an Acoustic Black Hole termination, *J. Sound Vib.* 349 (2015) 67–79.
- [14] T. Zhou, L. Tang, H. Ji, J. Qiu, L. Cheng, Dynamic and static properties of double-layered compound acoustic black hole structures, *Int. J. Appl. Mech.* 09 (2017) 1750074.
- [15] L. Ma, T. Zhou, L. Cheng, Acoustic black hole effects in thin-walled structures: realization and mechanisms, *J. Sound Vib.* 525 (2022) 116785.
- [16] S. Quaegebeur, G. Raze, L. Cheng, G. Kerschen, A virtual acoustic black hole on a cantilever beam, *J. Sound Vib.* 554 (2023) 117697.
- [17] T. Zhou, J.-D. Chazot, E. Perrey-Debain, L. Cheng, Performance of the partition of unity finite element method for the modeling of timoshenko beams, *Comput. Struct.* 222 (2019) 148–154.
- [18] Y. Ma, Z. Deng, A semi-analytical method for the dispersion analysis of orthotropic composite plates with periodically attached acoustic black hole resonators, *Appl. Math. Model.* 110 (2022) 562–582.
- [19] L. Tang, N. Gao, J. Xu, K. Chen, L. Cheng, A light-weight periodic plate with embedded acoustic black holes and bandgaps for broadband sound radiation reduction, *J. Acoust. Soc. Am.* 150 (2021) 3532–3543.
- [20] H. Ji, B. Han, L. Cheng, D.J. Inman, J. Qiu, Frequency attenuation band with low vibration transmission in a finite-size plate strip embedded with 2D acoustic black holes, *Mech. Syst. Signal Process.* 163 (2022) 108149.
- [21] H. Ji, N. Wang, C. Zhang, X. Wang, L. Cheng, J. Qiu, A vibration absorber based on two-dimensional acoustic black holes, *J. Sound Vib.* 500 (2021) 116024.
- [22] T. Zhou, L. Cheng, Planar swirl-shaped acoustic black hole absorbers for multi-directional vibration suppression, *J. Sound Vib.* 516 (2022) 116500.
- [23] K. Hook, J. Cheer, S. Daley, A parametric study of an acoustic black hole on a beam, *J. Acoust. Soc. Am.* 145 (2019) 3488–3498.
- [24] W. Huang, C. Tao, H. Ji, J. Qiu, Enhancement of wave energy dissipation in two-dimensional acoustic black hole by simultaneous optimization of profile and damping layer, *J. Sound Vib.* 491 (2021) 115764.
- [25] Q. Fu, J. Wu, C. Yu, X. Du, N. Zhang, J. Zhang, Parametric studies and optimal design of the exponents collocation of a segmented acoustic black hole beam, *Appl. Acoust.* 200 (2022) 109086.
- [26] F.W. Williams, W.H. Wittrick, An automatic computational procedure for calculating natural frequencies of skeletal structures, *Int. J. Mech. Sci.* 12 (1970) 781–791.
- [27] J.R. Banerjee, F.W. Williams, Exact Bernoulli-Euler dynamic stiffness matrix for a range of tapered beams, *Int. J. Numer. Methods Eng.* 21 (1985) 2289–2302.

- [28] J.R. Banerjee, D.R. Jackson, Free vibration of a rotating tapered Rayleigh beam: a dynamic stiffness method of solution, *Comput. Struct.* 124 (2013) 11–20.
- [29] J.R. Banerjee, A. Ananthapuvirajah, Free flexural vibration of tapered beams, *Comput. Struct.* 224 (2019) 106106.
- [30] X. Liu, Y. Zhao, W. Zhou, J.R. Banerjee, Dynamic stiffness method for exact longitudinal free vibration of rods and trusses using simple and advanced theories, *Appl. Math. Model.* 104 (2022) 401–420.
- [31] X. Liu, L. Chang, J.R. Banerjee, H.-C. Dan, Closed-form dynamic stiffness formulation for exact modal analysis of tapered and functionally graded beams and their assemblies, *Int. J. Mech. Sci.* 214 (2022) 106887.
- [32] M. Ling, S. Wu, Z. Luo, L. Chen, T. Huang, An electromechanical dynamic stiffness matrix of piezoelectric stacks for systematic design of micro/nano motion actuators, *Smart Mater. Struct.* 32 (2023) 115012.
- [33] Z. Ba, J. Niu, Y. Liu, J. Liang, Dynamic response of a multi-scale layered saturated porous half-space due to seismic dislocation source by using a revised dynamic stiffness matrix method, *Appl. Math. Model.* 120 (2023) 217–245.
- [34] H. Sheng, M.-X. He, Q. Ding, Vibration suppression by mistuning acoustic black hole dynamic vibration absorbers, *J. Sound Vib.* 542 (2023) 117370.
- [35] J.Y. Lee, W. Jeon, Exact solution of Euler-Bernoulli equation for acoustic black holes via generalized hypergeometric differential equation, *J. Sound Vib.* 452 (2019) 191–204.
- [36] R. Beals, J. Szmigielski, G-Functions Meijer, A Gentle Introduction, *Not. Am. Math. Soc.* 60 (2013) 866.
- [37] B. Davies, *Integral Transforms and Their Applications*, Springer New York, New York, 2002.
- [38] F. Olver, D. Lozier, R. Boisvert, C. Clark, *The NIST Handbook of Mathematical Functions*, Cambridge University Press, New York, 2010.
- [39] C.S. Meijer, Über die Integraldarstellungen der whittakerschen funktion $W_{k,m}(z)$ und der hankelschen und besselschen funktionen, *Nieuw Arch. Voor Wiskd.* 18 (1936) 35–37.
- [40] W.H. Wittrick, F.W. Williams, A general algorithm for computing natural frequencies of elastic structures, *Q. J. Mech. Appl. Math.* 24 (1971) 263–284.
- [41] J.R. Banerjee, A. Ananthapuvirajah, An exact dynamic stiffness matrix for a beam incorporating Rayleigh–Love and Timoshenko theories, *Int. J. Mech. Sci.* 150 (2019) 337–347.
- [42] S. Quaegebeur, G. Raze, L. Cheng, G. Kerschen, A virtual acoustic black hole on a cantilever beam, *J. Sound Vib.* 554 (2023) 117697.